MWC 656 is unlikely to contain a black hole

Janssens, S.; Shenar, T.; Degenaar, N.; Bodensteiner, J.; Sana, H.; Audenaert, J.; Frost, A.J.

Citation for published version (APA):

Astronomy & Astrophysics

LETTER TO THE EDITOR

MWC 656 is unlikely to contain a black hole

S. Janssens[1], T. Shenar[2], N. Degenaar[2], J. Bodensteiner[3], H. Sana[1], J. Audenaert[1], and A. J. Frost[4]

[1] Institute of Astronomy, KU Leuven, Celestijnenlaan 200D, 3001 Leuven, Belgium
e-mail: `soetkin.janssens@kuleuven.be`
[2] Anton Pannekoek Institute for Astronomy, Science Park 904, 1098 XH Amsterdam, The Netherlands
[3] European Organisation for Astronomical Research in the Southern Hemisphere (ESO), Karl-Schwarzschild-Str 2, 85748 Garching, Germany
[4] European Southern Observatory, Alonso de Cordova 3107, Vitacura, Casilla 19001, Santiago de Chile, Chile

ABSTRACT

Contact. MWC 656 was reported to be the first known Be star with a black-hole (BH) companion on a 60 d period. The mass of the proposed BH companion is estimated to be between 4 and 7 $M_\odot$. This estimate is based on radial velocity (RV) measurements derived from the Fe II λ4583 emission line of the Be star disc and from the He II λ4686 emission line, assumed to be formed in a disc around the putative BH.
Aims. Using new high-resolution spectroscopic data, we investigate whether MWC 656 truly contains a BH.
Methods. We used the cross-correlation method to calculate the RVs of both the Be star and the He II λ4686 emission line to derive a new orbital solution. We also used a spectral disentangling method to look for the spectral signature of a companion.
Results. We derived an orbital period of 59.028 ± 0.011 d and a mass ratio of $q = M_{\rm He\,II}/M_{\rm Be} = 0.12 \pm 0.03$, much lower than the previously reported value of $q = 0.41 \pm 0.07$. By adopting a mass for the Be star of $M_{\rm Be} = 7.8 \pm 2.0\,M_\odot$, the mass of the companion is $0.94 \pm 0.34\,M_\odot$. For the upper limit of $M_{\rm Be} = 16\,M_\odot$ and $q = 0.15$, the mass of the companion is $2.4\,M_\odot$. Performing the disentangling on mock spectra shows that the spectral signature of a non-degenerate stellar companion with such a low mass cannot be retrieved using our data.
Conclusions. Our measurements do not support the presence of a BH companion in MWC 656. Rather, the derived upper limit on the mass of the companion indicates that it is either a neutron star, a white dwarf, or a hot helium star. Far-UV data will aid in rejecting or confirming a hot helium-star companion.

Key words. stars: individual: MWC 656 – stars: emission-line, Be – binaries: spectroscopic – stars: black holes

1. Introduction

Be stars are suggested to form through binary interactions (e.g., Bodensteiner et al. 2020b; Hastings et al. 2021; Dallas et al. 2022; Dufton et al. 2022). Therefore, Be-binaries offer unique opportunities to study binary interactions and their products. An important system of this type is MWC 656, also known as the first reported binary comprising a Be star and a black-hole (BH) companion, namely, a Be+BH binary (Casares et al. 2014, hereafter referred to as CNR14). However, a more recent study has refuted the BH scenario (Rivinius et al. 2022, hereafter referred to as RKC22).

It has been proposed that MWC 656 is a γ-ray binary candidate (Lucarelli et al. 2010) with an orbital period of 60.37 ± 0.04 d derived by photometry (Williams et al. 2010). The Be star has an effective temperature of $T_{\rm eff} = 19\,000 \pm 3000$ K (Williams et al. 2010) and a spectral type of B1.5-2 III (CNR14). Williams et al. (2010) has also suggested that the system might be a runaway, given its derived distance of 2.6 ± 1.0 kpc and its high Galactic latitude $b = -12°$.

A spectroscopic study of MWC 656 revealed the presence of He II λ4686 in emission (CNR14), which has been assumed to originate from an accretion disc around a hot companion. From an orbital fitting of radial velocity (RV) measurements of the Be star and He II λ4686, CNR14 derived an eccentricity of

$e = 0.10 \pm 0.04$ and a mass ratio of $q = M_{\rm comp}/M_{\rm Be} = 0.41 \pm 0.07$. With an adopted mass for the Be star between 10–16 $M_\odot$, they estimated a companion mass of 4–7 $M_\odot$. From the absence of spectral features associated with a luminous companion, these authors concluded that the companion is a BH. No Be+BH binaries had been reported in the literature prior to this, as most Be X-ray binaries have confirmed neutron-star (NS) companions or uncertain companions (Belczynski & Ziolkowski 2009).

MWC 656 was also detected as a faint X-ray source, with luminosities in line with the quiescent Be+BH scenario (Munar-Adrover et al. 2014; Ribó et al. 2017). Furthermore, the combined radio ($L_{8.6\,{\rm GHz}} \sim 10^{26}$–$10^{27}$ erg s^{-1}) and X-ray luminosities ($L_{1-10\,{\rm keV}} \sim 10^{30}$–$10^{31}$ erg s^{-1}) are in agreement with those for low-mass quiescent X-ray binaries containing a BH (Dzib et al. 2015; Ribó et al. 2017). As suggested by Zamanov et al. (2016), the BH is expected to constantly accrete from the outer edges of the Be disc, which would give rise to the low detected X-ray luminosities and the quiescent appearance.

However, a more recent spectroscopic study suggested that MWC 656 hosts a hot subdwarf (sdO) rather than a BH (RKC22). RKC22 found a RV semi-amplitude for He II λ4686 similar to CNR14 ($K_{\rm He\,II} \sim 80$ km s^{-1}). However, the RV semi-amplitudes for the Be star are discrepant.

CNR14 used the Fe II λ4583 emission line to obtain RVs for the Be star and found $K_{\rm Be} = 32.0 \pm 5.3$ km s^{-1}, whereas

RKC22 used the He I λ6678 atmospheric absorption line finding $K_{Be} = 10$–$15\,km\,s^{-1}$, thus lowering the mass of the secondary by a factor of about two to three. Hence, RKC22 ruled out a BH companion. If the companion is indeed not a BH, the number of detected Be+BH binaries falls back to zero. In addition, the suggestion that Be stars may form through common envelope has to be revised (Grudzinska et al. 2015).

In this Letter, we present a full orbital analysis of MWC 656 based on new high-resolution spectra and we re-evaluate the nature of the companion in the system. Section 2 describes the data. Section 3 presents the orbital and spectral disentangling analysis. We discuss our results in Sect. 4 and present our conclusions in Sect. 5.

2. Spectroscopic data

2.1. New high-resolution data

New spectroscopic data were obtained with the High-Efficiency and high-Resolution Mercator Echelle Spectrograph (HERMES) instrument, mounted on the 1.2-m *Mercator* Telescope at the Roque de los Muchachos observatory on the Canary island La Palma, Spain (Raskin et al. 2011). The high-resolution mode has a resolving power of $R = \lambda/\Delta\lambda \simeq 85\,000$ and covers the wavelength range 3800–9000 Å with a step size of ~0.02−0.05 Å.

We obtained 18 HERMES spectra with signal-to-noise (S/N) ratios around 50–60 per pixel. The dates of observation and S/N of each spectrum can be found in Table 1. The normalisation was done with a spline interpolation using the Python package SciPy (Virtanen et al. 2020). Parts of the spectra are shown in Fig. B.1.

2.2. Archival data

We also retrieved the 34 archival spectra used by CNR14. These data were taken with the Fibre-fed RObotic Dual-beam Optical Spectrograph (FRODOspec; Morales-Rueda et al. 2004), mounted on the 2.0-m Liverpool Telescope (LT), which is also located at the Roque de Los Muchachos Observatory. The data have $R \sim 5500$ and cover the wavelength range 3900–5215 Å with a step size of ~0.4 Å. Most of the data were taken between April-July 2011 and four spectra were taken in May–June 2012. The data generally have $S/N > 200$ per pixel. The normalisation was done similarly to the HERMES spectra.

3. Analysis

3.1. Radial velocity measurements

We determined the RVs through iterative cross-correlation. By cross-correlating a template over part of the spectra, a cross-correlation function (CCF) can be calculated. A parabola fit to the CCF then determines the RV of the spectrum (Zucker 2003). We also used Gaussian fitting following Sana et al. (2013) and obtained very similar results.

For the cross-correlation, the first spectrum was chosen as the initial template. Every iteration creates a master template by coadding the spectra according to the derived RVs. This master template is then used in the next iteration. The obtained RVs are relative to the master template spectrum and hence no systemic velocity is derived. Iterations stopped when RVs converged.

For the Be star, we derived RVs in three different regions: a set of He I absorption lines that were fitted simultaneously, the Hβ emission line, and the Fe II λ4583 emission line (also used by CNR14). The set of He I absorption lines includes He I λλ4026,

Table 1. Mid-exposure baricentric Julian dates (BJD), exposure times, and S/N of the HERMES spectra of MWC 656.

BJD	Exp. time [s]	S/N at Hα	Phase
2456227.456	900	57	0.29
2456647.321	580	53	0.40
2457659.462	1200	56	0.55
2457663.402	1200	49	0.61
2459053.691	900	59	0.17
2459057.692	900	54	0.23
2459060.618	900	59	0.28
2459077.606	900	62	0.57
2459081.566	900	59	0.64
2459094.506	900	62	0.86
2459096.467	900	65	0.89
2459102.410	900	69	0.99
2459119.538	900	56	0.28
2459130.500	900	61	0.47
2459384.721	600	49	0.77
2459426.569	720	62	0.48
2459462.614	1350	51	0.09
2459733.687	670	56	0.69

Notes. The last column also indicates the corresponding phase in the derived 59.028 d orbit (see Sect. 3.2).

4121, 4144, 4388, 4471, 4713, and 5048. We did not include He I λ5876 or He I λ6678 + He II λ6683 as they seem to have contamination from another emission component (see Fig. C.1, middle and right panels). We also obtained RVs for He II λ4686. The RVs are listed in Table A.1 with a 1σ error.

3.2. Orbital fitting

The orbital fitting was performed using the spinOS tool, which uses a non-linear least squares minimisation[1]. We fitted the orbital period, P, time of periastron passage, T_0, eccentricity, e, argument of periastron, ω (implemented in spinOS with respect to the ascending node), and the RV semi-amplitude of the Be star (K_{Be}) and of the companion ($K_{He\,II}$). The systemic velocities of each component were also fitted. However, as mentioned in Sect. 3.1, they have no physical meaning here and we refer to them as the zero-point offsets zo_{Be} and $zo_{He\,II}$.

The orbital solutions are listed in Table 2 with their 1σ error. The first column lists a solution allowing for non-zero eccentricity. However, according to the Lucy–Sweeney test ($e/\sigma_e < 2.4$; Lucy & Sweeney 1971), the obtained eccentricity is not significant and for the remainder of the manuscript, we assume that the system is circular.

The circular orbital solutions obtained from the He I absorption lines, Hβ, and Fe II λ4583 are all in agreement with each other, suggesting that our results are robust over different spectral lines. The orbital solutions obtained for each of the two components individually are also in agreement (see Table 3).

We also performed a fit using both the HERMES and LT data. However, when performing cross-correlation on the He I absorption lines in the LT data, the RVs show large scatter. While looking at the He I absorption lines individually, we noticed that the zero-point of each line is different, probably due to a non-linear wavelength calibration issue in the data. As a result, this leads to issues when fitting multiple lines together. Therefore,

---

[1] https://github.com/matthiasfabry/spinOS

Table 2. Orbital and dynamical parameters of MWC 656.

Used Be line	He I absorption lines[*]		Hβ	Fe II λ4583	HERMES + LT (He II)
P [d]	59.085 ± 0.026	59.094 ± 0.024	59.090 ± 0.033	59.094 ± 0.029	59.028 ± 0.011
T_0 [BJD-2450000]	7510.0 ± 8.5	7507.53 ± 0.61	7507.69 ± 0.84	7507.58 ± 0.75	7509.20 ± 0.31
e	0.037 ± 0.035	0 (fixed)	0 (fixed)	0 (fixed)	0 (fixed)
ω [°]	105 ± 51	90 (fixed)	90 (fixed)	90 (fixed)	90 (fixed)
K_{Be} [km s^{-1}]	11.5 ± 2.8	11.5 ± 2.8	9.8 ± 2.0	11.7 ± 2.6	11.6 ± 3.7
$K_{He\,II}$ [km s^{-1}]	92.6 ± 3.1	92.9 ± 3.0	92.7 ± 4.2	92.8 ± 3.7	91.2 ± 2.9
$q = K_1/K_{He\,II}$	0.12 ± 0.03	0.12 ± 0.03	0.11 ± 0.02	0.13 ± 0.03	0.13 ± 0.05
zo$_{Be}$ [km s^{-1}]	−14.5 ± 2.1	−14.5 ± 2.1	−13.7 ± 1.4	−32.0 ± 1.9	−14.8 ± 2.8
zo$_{He\,II}$ [km s^{-1}]	85.1 ± 2.3	85.2 ± 2.2	85.3 ± 3.1	85.2 ± 2.7	87.2 ± 2.8
ΔRV [km s^{-1}]	/	/	/	/	30.0 ± 4.1
Reduced χ^2	10.6	10.3	19.8	15.5	18.7

Notes. Only the last column includes LT data in the fit. [*]Lines included in the cross-correlation range: He I λλ4026, 4121, 4144, 4388, 4471, 4713, 5048.

Table 3. Orbital and dynamical parameters obtained from each component individually.

Used line	He I absorption[*]	He II λ4686
P [d]	58.906 ± 0.092	59.098 ± 0.032
T_0 [BJD-2450000]	7511.7 ± 2.4	7477.89 ± 0.84[**]
e	0 (fixed)	0 (fixed)
ω [°]	90 (fixed)	90 (fixed)
K [km s^{-1}]	11.8 ± 1.3	93.0 ± 4.1
zo [km s^{-1}]	−15.08 ± 0.94	85.0 ± 3.0
Reduced χ^2	3.9	18.9

Notes. [*]Lines included in the cross-correlation range: He I λλ4026, 4121, 4144, 4388, 4471, 4713, 5048 [**]The ~30 day difference with respect to all other orbital solutions originates in using the secondary as the primary.
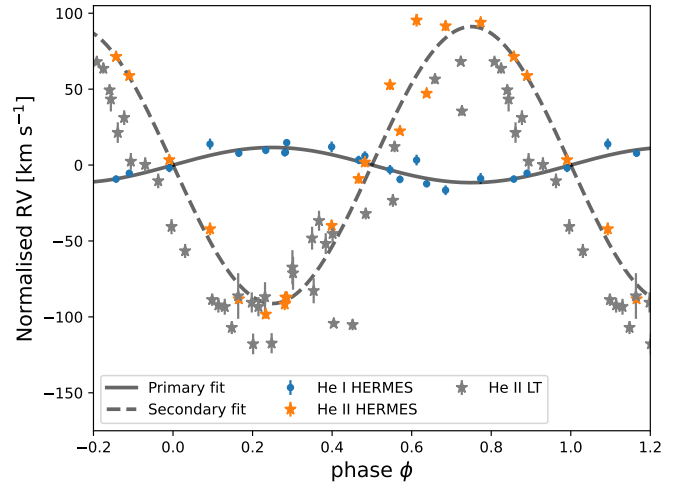

Fig. 1. Orbital fit using $P = 59.028$ d and $T_0 = 2457509.20$. The RVs of each component are subtracted by their respective zo from the HERMES + LT fit.

we did not include the RVs from the He I lines in the LT spectra in the HERMES + LT orbital fitting.

The HERMES + LT orbital solution is listed in the final column of Table 2 and is shown in Fig. 1. It can be seen that there is an offset between the HERMES and LT He II measurements, potentially attributed due to the wavelength calibration issue in the LT data. Therefore, we fitted an orbital solution including a RV shift ΔRV between the HERMES and LT data using a Levenberg–Marquardt optimisation method (see Sana et al. 2013). While fitting for ΔRV, we lowered the precision of the semi-amplitudes and mass ratio. However, combining both sets of data does allow for an improvement in P and T_0. Therefore, for the remainder of the study, we only used P and T_0 from the HERMES + LT fit and all other parameters from the circular fit on the He I lines, since the use of absorption lines is generally preferred over the emission lines.

The orbital period that we derived ($P \simeq 59$ d) is slightly smaller than the one used by CNR14, but this difference is still significant. The derived mass ratio of $q = 0.12 \pm 0.03$ is much lower than the previously reported value of $q = 0.41 \pm 0.07$ (CNR14). Combining our mass ratio with a mass of $7.8 \pm 2.0\,M_\odot$ for the Be star (Williams et al. 2010), the mass of the companion is $0.94 \pm 0.34\,M_\odot$. This mass range is in agreement with a low-mass main-sequence star, white dwarf (WD), and sdO companion. However, it is not massive enough for a BH ($M \gtrsim 2.5\,M_\odot$). Even when the mass of the Be star would be $16\,M_\odot$, which is the upper limit proposed by CNR14, and the mass ratio would

be 0.15, the mass of the companion would be $2.4\,M_\odot$; hence, it would still not be in the BH–mass range. Therefore, it is highly unlikely that MWC 656 hosts a BH. However, a neutron-star (NS) companion seems possible. We further discuss the different possibilities in Sect. 4.2.

Our derived orbital solutions for He I and Fe II agree with each other and with the RV semi-amplitude mentioned in RKC22. To investigate the cause of the discrepancy between the RV semi-amplitude of Fe II ($K_{Fe\,II}$) derived here and the one derived by CNR14, we also measured RVs for Fe II λ4583 in the LT data using both cross-correlation and double-Gaussian fitting. In both cases, we find $K_{Fe\,II} \approx 18$ km s^{-1}, with a larger dispersion (3 km s^{-1} vs. 4 km s^{-1}) for the Gaussian-fitting method. This is in contrast with both the value listed in CNR14 and the one obtained from the HERMES data. The discrepancy with the latter might be due to the resolution of the data, however, HERMES and LT agree within 1.5σ. At present, we cannot explain the discrepancy with CNR14.

3.3. Spectral disentangling

Spectral disentangling can reveal the signature of companions two orders of magnitudes fainter than the primary star
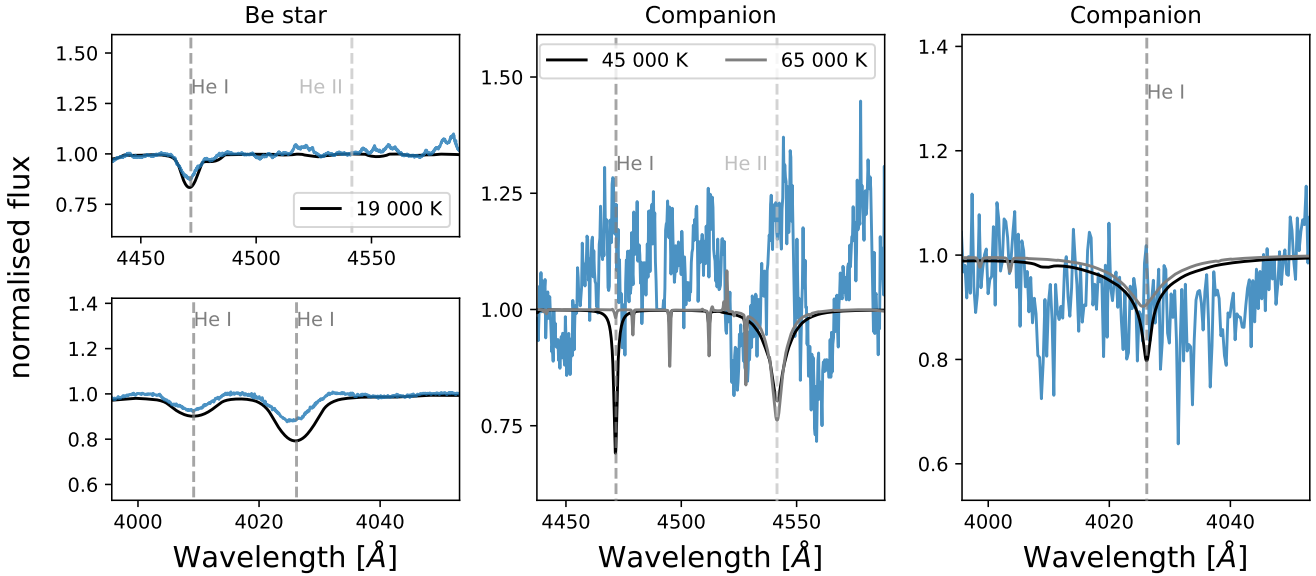
Fig. 2. Disentangled spectrum (blue) for the primary (Be star, left panels) and the companion (middle and right panel). The model in the left panels (black) is for a B star of 19 000 K with $v \sin i = 330 \, \mathrm{km \, s^{-1}}$. The models in the middle and right panels are for a stripped star of 45 000 K (black) and 65 000 K (grey) with $v \sin i = 30 \, \mathrm{km \, s^{-1}}$. Emission features in the top-left panel are mostly due to iron.

with a good quality data set. Thus, we can push the detection of companions down to very low light ratios (see e.g., Bodensteiner et al. 2020a; Shenar et al. 2020, 2022).

We used the iterative shift-and-add technique[2] (González & Levato 2006; Shenar et al. 2020, 2022), fixing the orbital parameters to the values we derived in Table 2. Figure 2 shows the disentangled spectra zoomed in on the regions of interest.

Due to strong variability in the emission lines, we avoid regions such as the Balmer and Paschen lines as well as the He II $\lambda 4686$ line. When excluding Balmer lines from the disentangling, we are not able to detect a WD companion. Even if we would be able to disentangle the Balmer lines, a WD would contribute an estimated $\sim 0.04\%$ to the optical spectra, which is too faint to be detected with the current data.

To determine whether a stripped star could be detected in this system, we performed disentangling on mock spectra. However, these simulations showed that neither a lowest-mass (1 $M_\odot$) nor a most massive ($\sim 2.5 \, M_\odot$) stripped star can be unambiguously detected (see Appendix D). Indeed, there is no clear signature of a companion detected in our data (Fig. 2).

4. Discussion

4.1. Considering whether the He II emission line originates from a disc around the companion

The shape of Hα is very variable and it often varies from a double-peak shape, which is indicative of a perturbed outer disc (see e.g., Zamanov et al. 2022). This supports the estimation that the companion is orbiting through the outer edges of the Be-disk (Zamanov et al. 2016), implying that an accretion disk may form.

In principle, it could also be the case that the hot (see Sect. 4.2) companion orbiting around the Be star heats up part of the Be disc (see also Fig. 8 in Peters et al. 2008, for the example of FY CMa). In this scenario, the He II $\lambda 4686$ (and He I $\lambda 6678$ + He II $\lambda 6683$ and He I $\lambda 5875$) emission line form in

the Be disc. Hence, the obtained RVs from the He II line could not be used to constrain the mass of the companion.

While He II is variable in shape, several epochs show a double-peaked feature (e.g., the grey spectrum in the top-right panel of Fig. B.1), suggesting a Keplerian disc. If part of the Be disc would be heated up, it seems rather unlikely that the shape of the emission line resembles that of a Keplerian disc.

For the same reason, the He emission lines most likely not originate from stellar winds; however, if they did indeed come from stellar winds, the derived RVs would still trace the motion of the hot companion. Therefore, we suggest that the He emission lines originate from an accretion disc around the hot companion.

4.2. Nature of the unseen companion

In Sect. 3.2, we explain that the companion is either a low-mass main-sequence star, WD, sdO, or NS. The presence of He II emission indicates a hot companion. A low-mass main-sequence companion with a mass $<2.5 \, M_\odot$ would then be $T_{\mathrm{eff}} \lesssim 10\,000 \, \mathrm{K}$ and is thus far too cool to be responsible for the He II emission so, we can exclude this possibility.

Any viable scenario must also be able to explain the system's radio and X-ray emission (Munar-Adrover et al. 2014; Dzib et al. 2015; Ribó et al. 2017). Be stars exhibit X-ray luminosities of $\sim 10^{29} - 10^{31} \, \mathrm{erg \, s^{-1}}$ (e.g., Nazé & Motch 2018) and radio luminosities of $\sim 10^{26} - 10^{27} \, \mathrm{erg \, s^{-1}}$ (e.g., Taylor et al. 1990) that may originate from the Be disc or wind. The presence of an sdO or accreting compact companion can also cause X-ray and radio emission in the range observed for MWC 656.

Below, we investigate whether a WD, sdO, or NS companion agree with the observed spectral features as well as the detected X-ray and radio. We do not discuss the γ-rays in detail, since they might be attributed to another source (see Alexander & McSwain 2015; Munar-Adrover et al. 2016).

4.2.1. A white dwarf

If the companion is a WD, it could be a candidate for a type Ia supernova progenitor. While the companion is currently

---

[2] https://github.com/TomerShenar/Disentangling_Shift_And_Add

accreting at low levels from the disc, the accretion rate might significantly increase during the evolution of the Be star. From an evolutionary perspective, the WD scenario seems the most likely, with an estimated 70% of all Be stars having a WD companion (van Bever & Vanbeveren 1997; Raguzova 2001). While no Be + WD binaries have been found in the Milky Way, some have been reported in the Magellanic Clouds (see Kahabka et al. 2006; Sturm et al. 2012; Coe et al. 2020). Furthermore, the presence of He II $\lambda4686$ emission was already reported in several binaries containing accreting WDs (such as in (magnetic) cataclysmic variables, e.g., Oliveira et al. 2017; Mason et al. 2019; Hou et al. 2023). However, it seems that these systems show Balmer emission at least as strong as the He II $\lambda4686$ emission, which does not seem to be the case here. The X-ray and radio luminosity of MWC 656 are both in the realm of values detected for the brightest accreting (magnetic) white dwarfs (Coppejans & Knigge 2020; Hewitt et al. 2020).

4.2.2. A hot subdwarf

MWC 656 shows striking similarities with previously detected Be + sdO binaries (such as e.g., ϕ Per Poeckert 1981, FY CMa Peters et al. 2008, o Pup Koubský et al. 2012, HD 55606 Chojnowski et al. 2018). MWC 656 shows strong Ca II $\lambda\lambda8202$, 8249, 8255 emission lines (see bottom panel of Fig. B.1), also detected in o Pup and HD 55606. Furthermore, just as in several studied Be + sdO binaries, there is additional emission visible in He I $\lambda6678$ + He II $\lambda6683$ and He I $\lambda5875$ (Fig. C.1 top, middle and right panels) tracing the same RV motion as the He II $\lambda4686$ emission line (Fig. C.1 top-left panel). So far, He II $\lambda4686$ emission has only been detected in ϕ Per and 59 Cyg (Rivinius & Štefl 2000). In both cases, the emission is very weak.

The X-ray luminosity of MWC 656 is in line with that observed for known Be + sdO binaries (Nazé et al. 2022). The detected radio luminosity also roughly agrees with other Be + sdO systems (Wendker 1995, 2015).

4.2.3. A neutron star companion

As suggested by Williams et al. (2010), MWC 656 might be a runaway. This could indicate a past supernova kick from a companion. However, a kick is also expected to introduce eccentricity. The circular orbit could be explained by an electron-capture supernova (Podsiadlowski et al. 2004). In this scenario, the potential runaway status of MWC 656 is probably due to a dynamical ejection.

The X-ray spectrum of MWC 656 (Munar-Adrover et al. 2014), consisting of a soft thermal emission component ($kT_{bb} \sim 0.1\,\mathrm{keV}$) and a harder emission tail (described as a $\Gamma \sim 1$ powerlaw), is not unlike that of neutron stars Be X-ray binaries observed at similarly low X-ray luminosities (e.g., Rouco Escorial et al. 2019; Tsygankov et al. 2020). The radio emission from Be + NS systems has not been explored in this regime (van den Eijnden et al. 2021).

5. Conclusion

Based on new high-resolution spectroscopic data, we investigated the nature of the companion to the Be star in the MWC 656 system. We find a mass ratio of $q = 0.12 \pm 0.03$, much lower than the previously reported $q = 0.41 \pm 0.07$.

A BH companion is thus ruled out by our analysis, in line with the findings of RKC22. We suggest that this discrepancy

with CNR14 can be due to the higher resolution of the data as well as the method used to derive the RVs.

The most likely companions are a sdO, WD, or NS. On the one hand, the circular orbit might indicate a sdO or WD companion. On the other hand, the position on the sky might indicate a runaway and, hence, favour the NS scenario. Given the spectroscopic, X-ray, and radio data, we do not favour any possibility more than the other. We note that if MWC 656 were to host:

- a NS, the low eccentricity is very unique and hints towards an electron-capture supernova;
- a sdO, it would add one more to the very few known Be+sdO binaries, which are extremely valuable in studying close binary interactions;
- a WD, then it might be a Type Ia supernova candidate.

Hence, any of the three companions would offer an exciting result. Upcoming far-UV data could tell us more about the nature of the companion, offering the possibility to either confirm or reject an sdO companion.

References

Alexander, M. J., & McSwain, M. V. 2015, MNRAS, 449, 1686
Belczynski, K., & Ziolkowski, J. 2009, ApJ, 707, 870
Bodensteiner, J., Shenar, T., Mahy, L., et al. 2020a, A&A, 641, A43
Bodensteiner, J., Shenar, T., & Sana, H. 2020b, A&A, 641, A42
Casares, J., Negueruela, I., Ribó, M., et al. 2014, Nature, 505, 378
Chojnowski, S. D., Labadie-Bartz, J., Rivinius, T., et al. 2018, ApJ, 865, 76
Coe, M. J., Kennea, J. A., Evans, P. A., & Udalski, A. 2020, MNRAS, 497, L50
Coppejans, D. L., & Knigge, C. 2020, New Astron. Rev., 89, 101540
Dallas, M. M., Oey, M. S., & Castro, N. 2022, ApJ, 936, 112
Dufton, P. L., Lennon, D. J., Villaseñor, J. I., et al. 2022, MNRAS, 512, 3331
Dzib, S. A., Massi, M., & Jaron, F. 2015, A&A, 580, L6
González, J. F., & Levato, H. 2006, A&A, 448, 283
Götberg, Y., de Mink, S. E., Groh, J. H., et al. 2018, A&A, 615, A78
Grudzinska, M., Belczynski, K., Casares, J., et al. 2015, MNRAS, 452, 2773
Hamann, W. R., & Gräfener, G. 2003, A&A, 410, 993
Hastings, B., Langer, N., Wang, C., Schootemeijer, A., & Milone, A. P. 2021, A&A, 653, A144
Hewitt, D. M., Pretorius, M. L., Woudt, P. A., et al. 2020, MNRAS, 496, 2542
Hou, W., Luo, A. L., Dong, Y.-Q., Chen, X.-L., & Bai, Z.-R. 2023, AJ, 165, 148
Kahabka, P., Haberl, F., Payne, J. L., & Filipović, M. D. 2006, A&A, 458, 285
Koubský, P., Kotková, L., Votruba, V., Šlechta, M., & Dvořáková, Š. 2012, A&A, 545, A121
Lanz, T., & Hubeny, I. 2007, ApJS, 169, 83
Lucarelli, F., Verrecchia, F., Striani, E., et al. 2010, ATel, 2761, 1
Lucy, L. B., & Sweeney, M. A. 1971, AJ, 76, 544
Mason, P. A., Wells, N. K., Motsoaledi, M., Szkody, P., & Gonzalez, E. 2019, MNRAS, 488, 2881
Morales-Rueda, L., Carter, D., Steele, I. A., Charles, P. A., & Worswick, S. 2004, Astron. Nachr., 325, 215
Munar-Adrover, P., Paredes, J. M., Ribó, M., et al. 2014, ApJ, 786, L11
Munar-Adrover, P., Sabatini, S., Piano, G., et al. 2016, ApJ, 829, 101
Nazé, Y., & Motch, C. 2018, A&A, 619, A148
Nazé, Y., Rauw, G., Smith, M. A., & Motch, C. 2022, MNRAS, 516, 3366
Oliveira, A. S., Rodrigues, C. V., Cieslinski, D., et al. 2017, AJ, 153, 144
Peters, G. J., Gies, D. R., Grundstrom, E. D., & McSwain, M. V. 2008, ApJ, 686, 1280
Podsiadlowski, P., Langer, N., Poelarends, A. J. T., et al. 2004, ApJ, 612, 1044

Poeckert, R. 1981, PASP, 93, 297

Raguzova, N. V. 2001, A&A, 367, 848

Raskin, G., van Winckel, H., Hensberge, H., et al. 2011, A&A, 526, A69

Ribó, M., Munar-Adrover, P., Paredes, J. M., et al. 2017, ApJ, 835, L33

Rivinius, Th., Klement, R., Chojnowski, S. D., et al. 2022, ArXiv e-prints [arXiv:2208.12315]

Rivinius, T., & Štefl, S. 2000, in IAU Colloq. 175: The Be Phenomenon in Early-Type Stars, eds. M. A. Smith, H. F. Henrichs, & J. Fabregat, ASP Conf. Ser., 214, 581

Rouco Escorial, A., Wijnands, R., Ootes, L. S., et al. 2019, A&A, 630, A105

Sana, H., Le Bouquin, J. B., Mahy, L., et al. 2013, A&A, 553, A131

Shenar, T., Bodensteiner, J., Abdul-Masih, M., et al. 2020, A&A, 639, L6

Shenar, T., Sana, H., Mahy, L., et al. 2022, A&A, 665, A148

Sturm, R., Haberl, F., Pietsch, W., et al. 2012, A&A, 537, A76

Taylor, A. R., Waters, L. B. F. M., Bjorkman, K. S., & Dougherty, S. M. 1990, A&A, 231, 453

Tsygankov, S. S., Doroshenko, V., Mushtukov, A. A., et al. 2020, A&A, 637, A33

van Bever, J., & Vanbeveren, D. 1997, A&A, 322, 116

van den Eijnden, J., Degenaar, N., Russell, T. D., et al. 2021, MNRAS, 507, 3899

Virtanen, P., Gommers, R., Oliphant, T. E., et al. 2020, Nat. Methods, 17, 261

Wendker, H. J. 1995, A&AS, 109, 177

Wendker, H. J. 2015, VizieR Online Data Catalog: VIII/99

Williams, S. J., Gies, D. R., Matson, R. A., et al. 2010, ApJ, 723, L93

Zamanov, R. K., Stoyanov, K. A., Martí, J., et al. 2016, A&A, 593, A97

Zamanov, R. K., Stoyanov, K. A., Marchev, D., et al. 2022, Astron. Nachr., 343

Zucker, S. 2003, MNRAS, 342, 1291

Appendix A: RV measurements

Table A.1 lists the measured RVs for the HERMES spectra.

Table A.1. Measured RVs for the given lines in each HERMES spectrum.

phase	bjd	$v_{\text{HeII}\lambda4686}$ [km s^{-1}]	v_{HeIlines} [km s^{-1}]	$v_{\text{H}\beta}$ [km s^{-1}]	$v_{\text{FeII}\lambda4583}$ [km s^{-1}]
0.093	2459462.614	45.1 ± 4.2	-1.0 ± 3.6	-17.6 ± 1.7	-26.1 ± 2.6
0.165	2459053.691	-1.0 ± 2.3	-7.0 ± 2.4	-0.1 ± 0.9	-17.6 ± 1.8
0.233	2459057.692	-11.1 ± 3.0	-5.1 ± 2.5	-2.6 ± 1.3	-27.2 ± 2.1
0.281	2459119.538	-4.4 ± 3.9	-6.6 ± 2.5	-2.8 ± 1.2	-21.1 ± 1.7
0.283	2459060.618	0.2 ± 2.9	-6.3 ± 2.3	-3.8 ± 1.3	-24.3 ± 1.5
0.286	2456227.456	0.0 ± 3.2	0.0 ± 2.3	0.0 ± 1.6	0.0 ± 2.9
0.399	2456647.321	47.3 ± 3.7	-2.8 ± 3.6	-9.6 ± 1.5	-32.5 ± 2.2
0.467	2459130.500	78.2 ± 3.3	-11.4 ± 2.8	-14.9 ± 1.0	-28.6 ± 2.1
0.482	2459426.569	89.1 ± 3.3	-8.8 ± 3.0	-16.2 ± 1.3	-29.1 ± 2.2
0.546	2457659.462	139.9 ± 3.3	-17.9 ± 3.1	-3.3 ± 2.3	-26.5 ± 2.4
0.571	2459077.606	109.6 ± 2.1	-24.2 ± 2.5	-20.5 ± 1.4	-40.5 ± 2.1
0.612	2457663.402	182.6 ± 4.2	-11.5 ± 3.5	-4.0 ± 1.8	-25.9 ± 2.9
0.638	2459081.566	134.4 ± 2.5	-27.1 ± 2.3	-21.4 ± 1.7	-36.6 ± 1.7
0.685	2459733.687	178.8 ± 3.4	-31.4 ± 3.2	-20.5 ± 1.7	-38.6 ± 2.3
0.773	2459384.721	181.2 ± 2.4	-23.6 ± 3.6	-17.5 ± 1.9	-60.6 ± 2.6
0.857	2459094.506	158.6 ± 1.8	-24.0 ± 2.3	-19.4 ± 1.2	-41.1 ± 1.6
0.890	2459096.467	146.0 ± 1.8	-20.2 ± 2.3	-22.3 ± 1.1	-47.0 ± 2.1
0.991	2459102.410	90.6 ± 2.1	-16.7 ± 2.8	-22.8 ± 0.9	-35.1 ± 1.6

Notes. Listed RVs are calibrated to have RV = 0 km s^{-1} for the spectrum taken at bjd = 2456227.456.

Appendix B: Spectral features

Figure B.1 shows several regions of the spectra of MWC 656.
Three spectra at phases 0.23, 0.77, and 0.98 are shown.
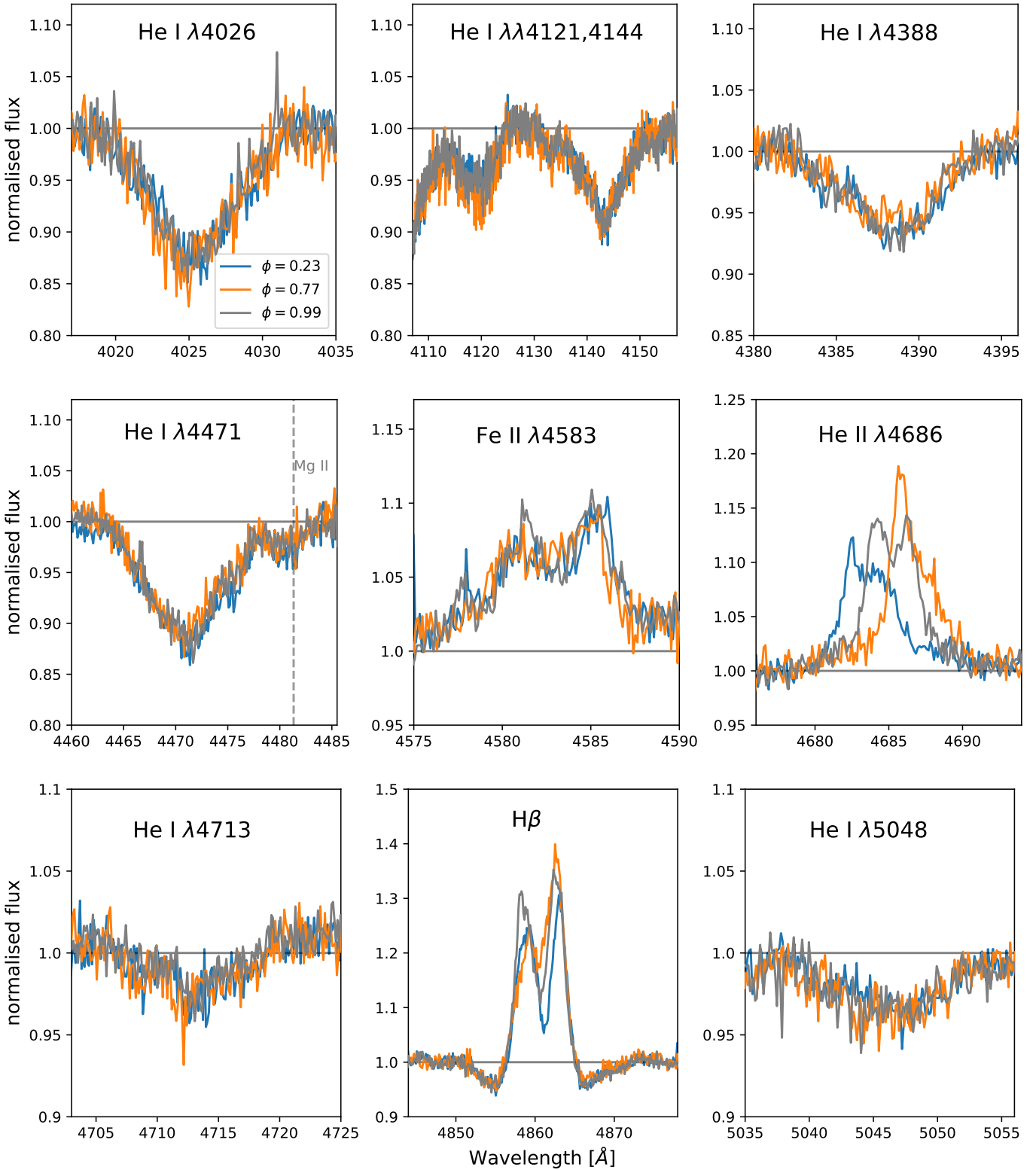

Fig. B.1. HERMES spectra of MWC 656 for phases corresponding to 0.23 (blue), 0.77 (orange), and 0.98 (grey). Each panel zooms in on a specific spectral line region, indicated in the individual panels. The left-most absorption feature in the panel of He I $\lambda\lambda$4121,4144 is part of the red wing of Hδ. The grey spectrum shows a clearly double peaked He II.
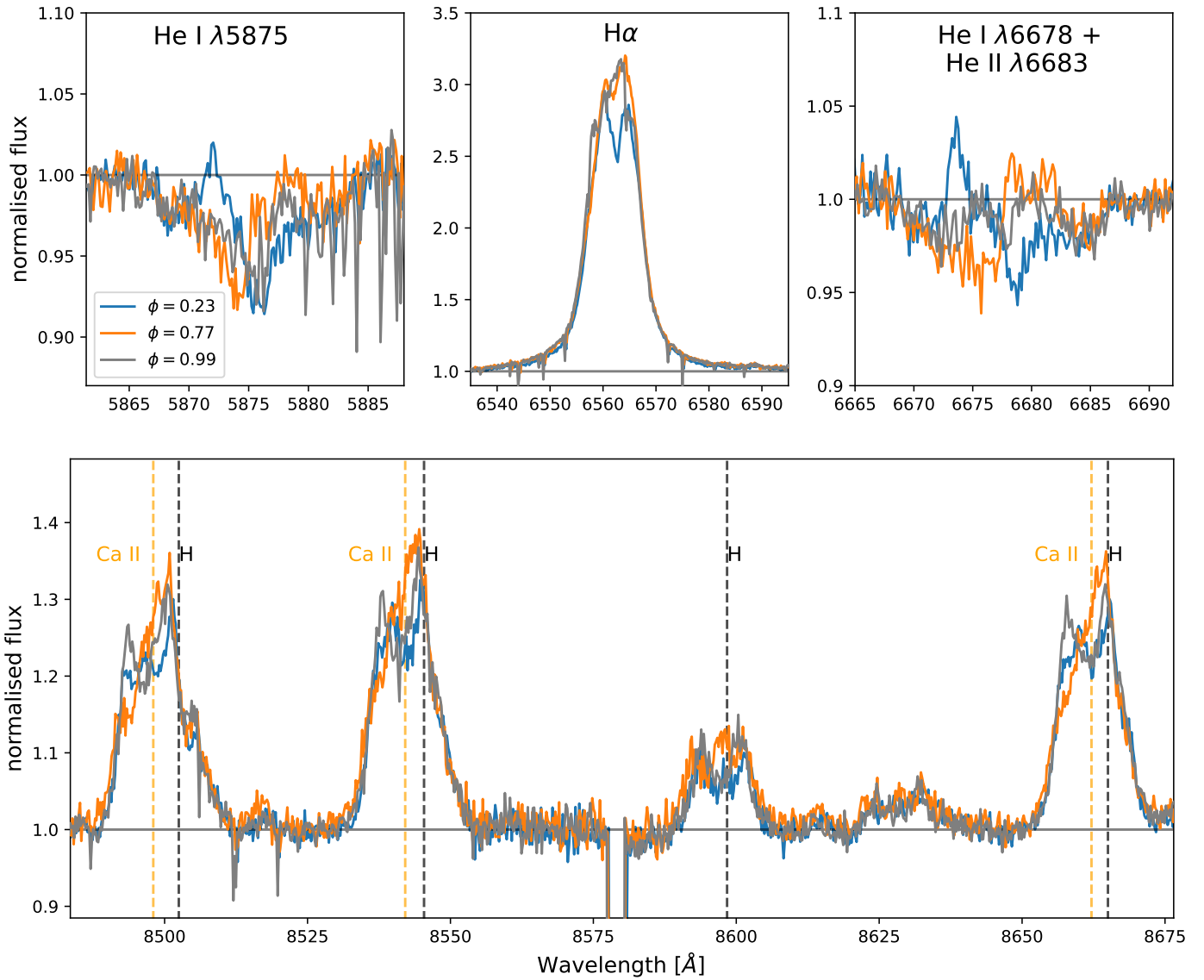
Fig. B.1. Continued. Panels with He I λ5875 and He I λ6678 + He II λ 6683 show clear blending with another emission component. The panel showing He I λ5875 is also contaminated by telluric lines. The bottom panel shows part of the Paschen series and the Ca II triplet.

Appendix C: Dynamical spectra

Figure C.1 shows the dynamical spectra of MWC 656 for
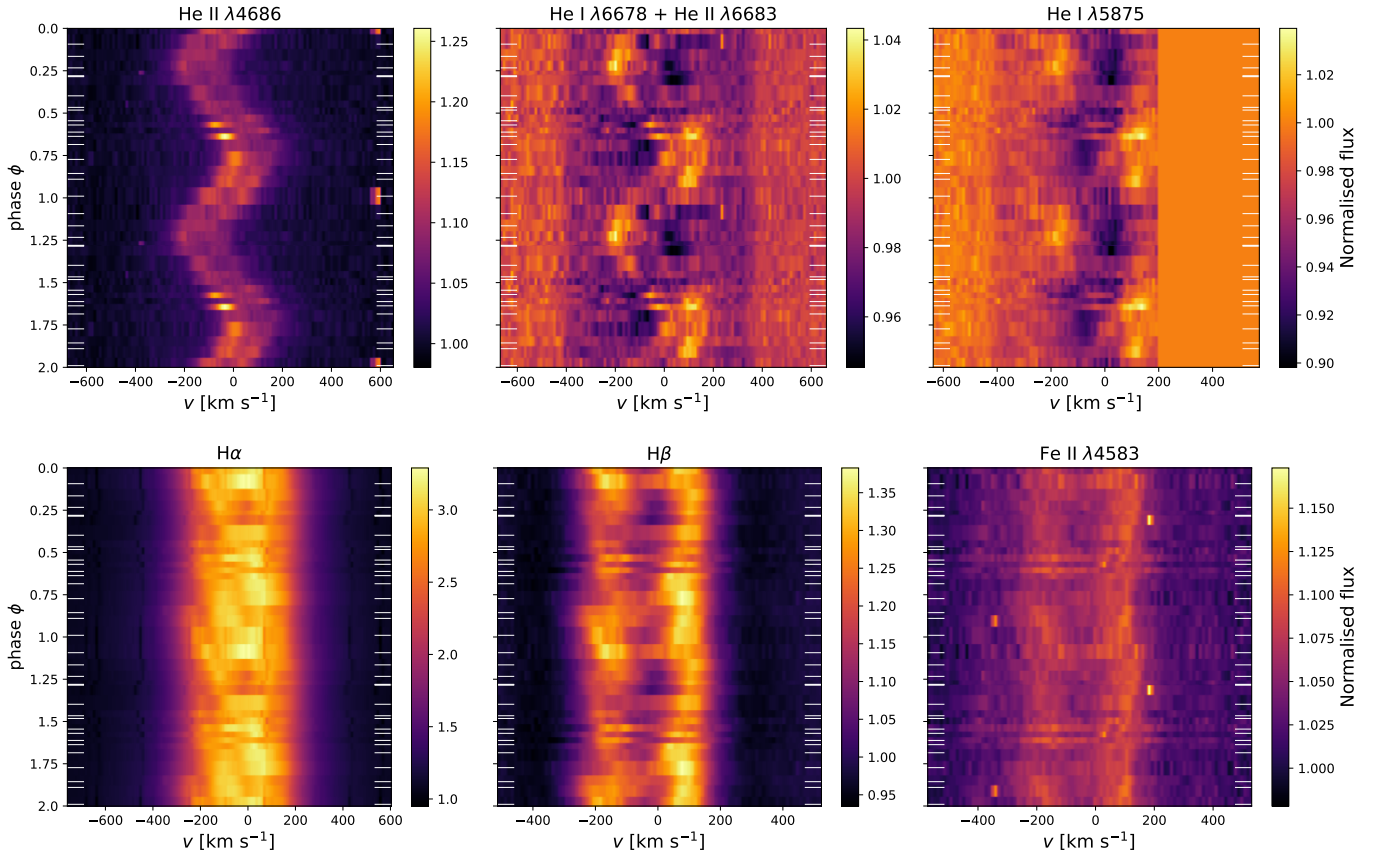different spectral lines.

Fig. C.1. Dynamical spectra of MWC 656. Phases are shown for two orbital periods. White horizontal bars indicate the phases at which HERMES spectra are taken. Top, from left to right: He ɪɪ λ4686, He ɪ λ6678 + He ɪɪ λ6683, He ɪ λ5875. Bottom, from left to right: Hα, Hβ, Fe ɪɪ λ4583. For He ɪ λ5875, part of the spectra where $v > 200\,\mathrm{km\,s^{-1}}$ is put equal to one because of telluric contamination and contamination from the interstellar Na ɪ line. Top-middle (He ɪ λ6678 + He ɪɪ λ6683) and -right (He ɪ λ5875) panels trace similar motion in emission as He ɪɪ λ4686 on top of the absorption coming from the Be star.

Appendix D: Testing the limits of spectral disentangling

Spectral disentangling is a useful tool for the detection of very faint companions and for putting constraints on the light ratio (e.g. Bodensteiner et al. 2020a; Shenar et al. 2020, 2022). However, if companions are too faint compared to the S/N of the spectroscopic data, even disentangling cannot aid in their detection. In order to test to which light ratios disentangling could detect a helium companion in MWC 656, we performed simulations on mock spectra.

For the Be star, the B-star spectrum was simulated with a TLUSTY (Lanz & Hubeny 2007) model spectrum of a 19 000 K star with $\log g = 4.00$ dex and $v \sin i = 330$ km s^{-1}. For the stripped star, we created models using the Potsdam Wolf-Rayet (PoWR) code (Hamann & Gräfener 2003) that agree with the expected parameters for the stripped star. The lowest possible mass of $1\,M_\odot$ yields parameters of $T_{\rm eff} \sim 45\,000$ K and $R \sim 0.4\,R_\odot$, while the upper mass limit of $\sim 2.5\,M_\odot$ results in a stripped star with $T_{\rm eff} \sim 60\,000$ K and $R \sim 0.6\,R_\odot$ (Götberg et al. 2018). Combining this with the parameters of the Be star, we estimate an optical contribution of the stripped

star between $\lesssim 1\%$ and $\sim 3\%$ for the lowest and highest mass, respectively.

As explained in Sect. 3.3, we did not disentangle the Balmer lines. Based on Figure 5 in Götberg et al. (2018), all stripped star models in the derived mass range seem to show absorption in He I(+II) $\lambda 4026$ and He II $\lambda 4542$. The lower mass models also show absorption in He I $\lambda 4472$. Therefore, we focused disentangling on these three lines.

For a stripped $1\,M_\odot$ star with $T_{\rm eff} = 45$ kK, we created mock spectra with a flux contribution for the stripped star of 1%, 3%, and 5%. A companion with a 3% light contribution would be detected using He I $\lambda 4471$ and He I(+II) $\lambda 4026$. However, the expected 1% contribution seems to be very challenging, as, for example, He I(+II) $\lambda 4026$ is not detected (see Fig. D.1).

For a $2.5\,M_\odot$ stripped star of $T_{\rm eff} = 60$ kK, we created mock spectra with a flux contribution for the stripped star of 3%, 5%, and 10%. Disentangling seems possible down to a flux contribution of 5%. However, the expected 3% flux contribution proves very challenging. While the He II $\lambda 4542$ seems detectable, again the He I(+II) $\lambda 4026$ is not detected (see Fig. D.2). Thus, based on simulations using mock spectra, we do not expect to be able to detect a stripped star companion using spectral disentangling.
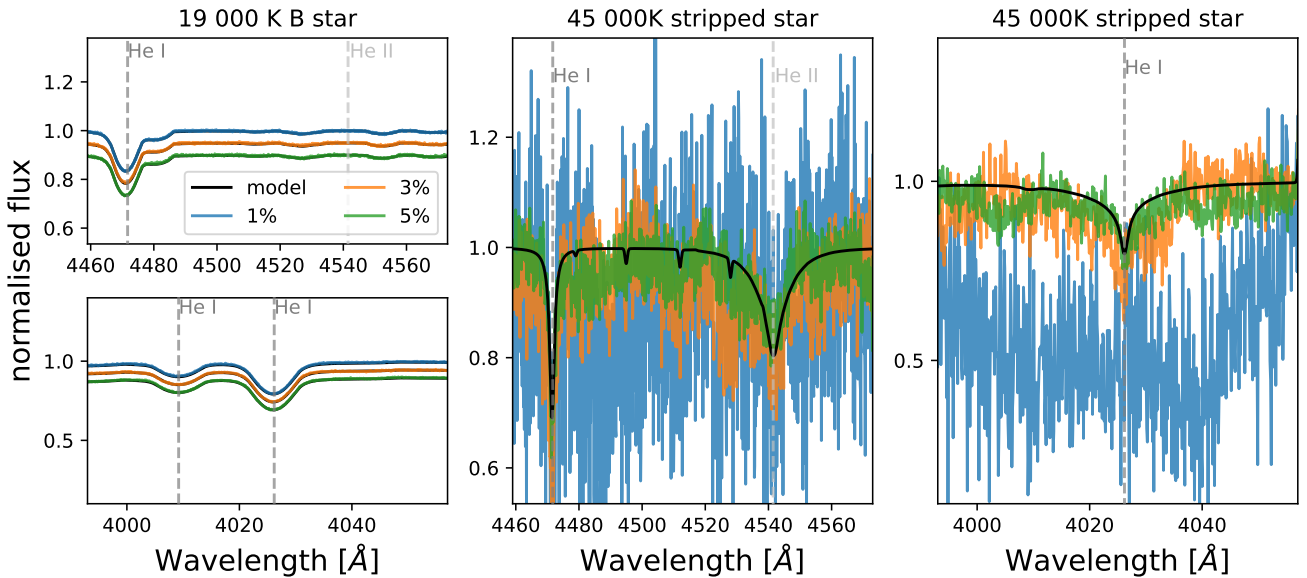

Fig. D.1. Disentangled simulated spectra for a 45 000 K stripped star with different contributions. Black: the models. Blue: the disentangled spectra given a 1% contributed flux. Orange: a 3% contributed flux. Green: for a 5% contributed flux. The model in the left panels is for a B star of 19 000 K and $v \sin i = 330$ km s^{-1}. The model in the middle and right panels is for a stripped star of 45 000 K and $v \sin i = 30$ km s^{-1}.
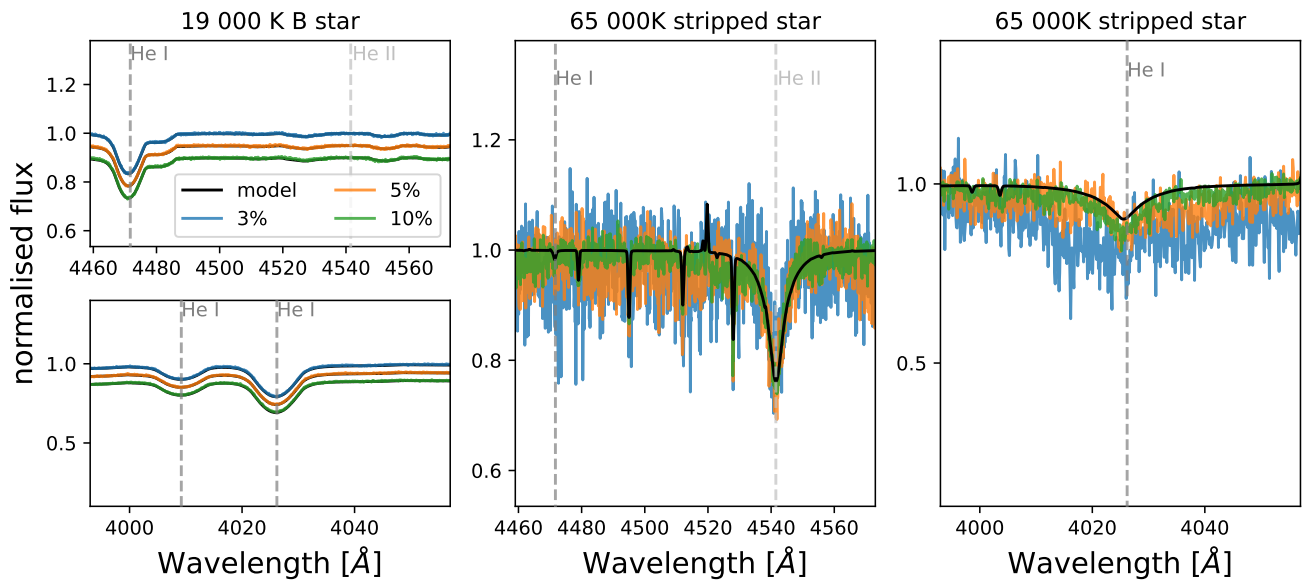
Fig. D.2. Same as Fig. D.1, but for a 65 000 K stripped star with a 3% (blue), 5% (orange), and 10% (green) contributed flux.